# A Low-Power, Wireless, Capacitive Sensing Frontend Based on a Self-Oscillating Inductive Link

Matthew Schormans, *Student Member, IEEE*, Virgilio Valente, *Member, IEEE*, and Andreas Demosthenous, *Fellow, IEEE*

***Abstract*— Wireless sensing systems are becoming popular in a range of applications, particularly in the case of biomedical circuits and food monitoring systems. A typical wireless sensing system, however, may require considerable complexity to perform the necessary analog to digital conversion and subsequent wireless transmission. Alternatively, in the case of inductive link based systems, large, manually operated impedance analyzers are required. Based on a detailed analysis of the link impedance, this paper proposes a simple method for wireless capacitive sensing through an inductive link that uses a self-oscillator and a frequency counter. The method enables changes in capacitance to be sensed and wirelessly transmitted simultaneously. In order to test the effectiveness of the method, a self-oscillating circuit was designed and fabricated in 0.18 $\mu$m CMOS, and combined with an on-chip humidity sensing capacitor. The system was tested in a humidity chamber across a range of 20–90%rh. Measured results from the system demonstrate that capacitive changes as small as 28 fF, translating to <2%rh, can be resolved, with a power consumption of 1.44 mW.**

***Index Terms*— Capacitive sensing, humidity sensing, inductive link, wireless sensing.**

## I. Introduction

WIRELESS sensing systems are becoming ubiquitous, particularly in biomedical and food monitoring applications. Biomedical application examples include neural monitoring [1], muscle pressure sensing [2], and glucose monitoring [3]. Some miniaturized devices can even perform multiple functions by incorporating multiple sensors on the same implant [4]. A food quality monitoring application in [5] has a passive receiver as part of an inductive link, but requires an impedance analyzer for interrogation. The same principle is demonstrated with a more general environmental sensor in [6], a biomedical pressure sensor in [7], and a humidity sensor in [8]. In all these cases an impedance analyzer is used to interrogate a passive resonant sensor.

Manuscript received January 22, 2018; revised April 10, 2018; accepted May 3, 2018. This work was supported by the Engineering and Physical Sciences Research Council (EPSRC) under Grants EP/K031953/1 and EP/M506448/1. This paper was recommended by Associate Editor E. Blokhina. *(Corresponding author: Matthew Schormans.)*

M. Schormans and A. Demosthenous are with the Department of Electronic and Electrical Engineering, University College London, London WC1E 7JE, U.K. (e-mail: matthew.schormans.10@ucl.ac.uk; a.demosthenous@ucl.ac.uk).

V. Valente was with the Department of Electronic and Electrical Engineering, University College London, London WC1E 7JE, U.K. He is now with the Department of Microelectronics, Delft University of Technology, 2628 Delft, The Netherlands (e-mail: v.valente@tudelft.nl).

Color versions of one or more of the figures in this paper are available online at http://ieeexplore.ieee.org.

Digital Object Identifier 10.1109/TCSI.2018.2835148

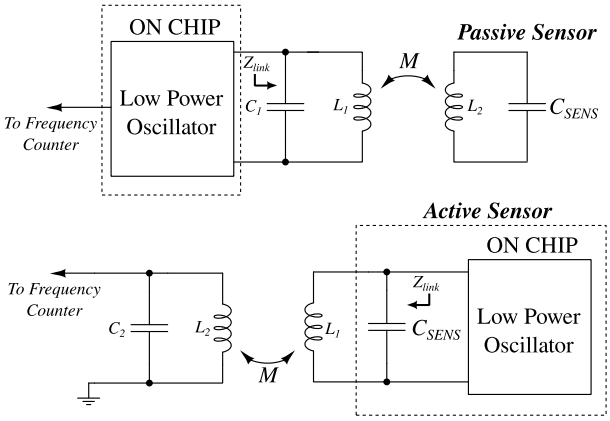


Fig. 1. Passive and active sensor configurations with the proposed system.

A typical signal chain of a wireless sensor might include: analog capacitive sensor interface, an analog to digital converter and microprocessor, and a wireless digital transmission method [9]–[13]. Alternatively for inductive link based systems, the signal chain consists of a capacitive sensor, an inductive link, and an impedance analyzer; generally implemented with large-scale lab equipment [5]–[8].

In contrast to these previous designs, this work proposes a simple method for implementing a wireless capacitive sensor frontend in a single circuit block. This approach has the benefit of being low power and highly miniaturized, particularly when compared with state of the art inductive link based wireless sensing systems [5]–[8].

The proposed system provides an integrated CMOS chip that allows interrogation of a capacitive sensor located at the primary or secondary side of an inductive link. The system can be used as an interrogator for a remote passive sensor, or as a transmitter in an active sensing device. Fig. 1 shows the two configurations that can be realised through this approach, referred to as active mode and passive mode. Capacitance to frequency conversion and wireless transmission are achieved in a single stage, by using a self-oscillator combined with an inductive link. Since passive mode allows for a remote sensor to be interrogated without an accompanying power source, it is well suited to applications where the power budget is critical, such as medical implants. Active mode would be more

suited to applications where power is more available, where it is desirable to have many active elements (rather than a single active element and many passive sensors) to reduce the effect of a circuit failure, e.g. in the case of industrial food monitoring.

The rest of the paper is structured as follows. Section II develops the inductive link theory required to describe the approach. Section III describes the design of the self-oscillating circuit, and Section IV presents measured results of the system. Concluding remarks and discussion are presented in Section V.

## II. Theory

The approach presented in this work bears some similarity to 'traditional' inductive sensing methods such as those described in [7], [8], and [14], but differs in terms of the basic principle of operation.

### A. The Phase-Dip Method

For wireless inductive sensing as shown in Fig. 2(a), an impedance analyzer uses a frequency sweep to determine the resonant characteristics of the link. Assuming that the link is highly asymmetric, i.e. $L_1 \ll L_2$ and $C_{stray}$ is negligible, a frequency sweep will yield a minimum in the phase plot (see Fig. 2(b)) approximately at the resonant frequency of the remote circuit formed by $L_2$ and $C_{SENS}$ [8], [15], where:

$$f_{dip} \approx \frac{1}{2\pi\sqrt{L_2 C_{SENS}}}. \tag{1}$$

Since $f_{dip}$ and $L_2$ are known, $C_{SENS}$ can be determined from (1). The component values for the arrangement in Fig. 2 are typical of values for a large loop and a small coil with many turns coupled within it. When attempting to miniaturize the system, $C_{stray}$ can no longer be ignored, and the approximation in (1) will no longer be valid.

Section II-B provides an exact analysis of $Z_{link}$ with the goal of an expression that can accurately determine $C_{SENS}$ for an arbitrary link, such that even a symmetric link can be successfully interrogated.

### B. Link Analysis to Determine an Exact Method

The proposed method determines the exact value of $C_{SENS}$, provided all other link parameters are known. Fig. 3 shows the general case of a parallel-parallel dual resonant inductive link. In the case of a miniaturized system, this is a more realistic representation of the link than that shown in Fig. 2(a), since $C_{stray}$ can no longer be ignored. By considering the circuit in Fig. 3 in general terms, the conclusions can be applied to a link where either $C_1$ or $C_2$ is used as $C_{SENS}$, i.e. the two cases of active and passive sensor (Fig. 1). Fig. 3 shows the impedance looking into the link $Z_{link}$, which is defined as follows:

$$Z_{link} = \left( \left( j\omega L_1 + R_1 + \frac{(\omega M)^2}{j\omega L_2 + \frac{1}{j\omega C_2} + R_2} \right)^{-1} + j\omega C_1 \right)^{-1} \tag{2}$$

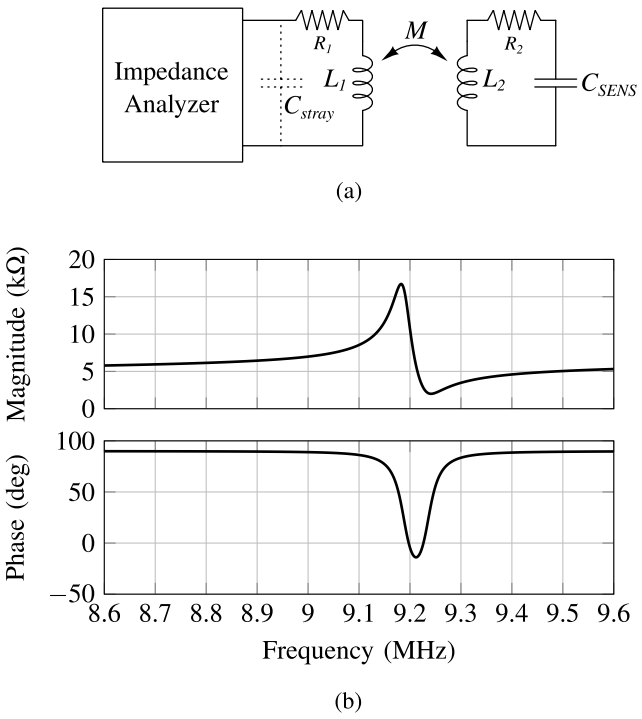


Fig. 2. The phase-dip measurement approach for wireless capacitive sensing. $L_1 = 10\ \mu$H, $L_2 = 100\ \mu$H, $R_{1,2} = 2\ \Omega$, $M = 3.162\ \mu$H, $C_{SENS} = 3$ pF. (a) Phase-dip measurement setup. (b) Example link impedance measurement.

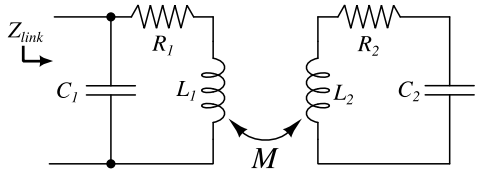


Fig. 3. General case inductive link model.

where $L_{1,2}$ are the primary and secondary link inductances, $C_{1,2}$ are the primary and secondary capacitances, $R_{1,2}$ are the primary and secondary coil losses, $M$ is the mutual inductance between the coils $L_{1,2}$, and $\omega$ is the angular frequency.

$Z_{link}$ is always considered as the impedance looking into the link from the point of view of the oscillator, which can be considered as a sinusoidal current source.

Fig. 4 shows the magnitude and phase plots of $Z_{link}$ for an example of a symmetric inductive link. The component values are given in the caption. These values are typical values that can be easily realised with small coils, and are comparable to the practical coils described in Section III. It shows that the approximation made in (1) is no longer valid for determining the value of $C_2$; calculating the result of (1) will not correlate to a 'dip' in the phase plot. In this way, a symmetric link can be considered as a worst case scenario for the phase-dip method, as both sides of the link play a significant part in determining the resonant frequency. The plots in Fig. 4 demonstrate the frequency-splitting phenomenon that occurs when $M$ is sufficiently large; this effect has been previously discussed and analyzed in the literature in detail [16]–[19]. The features of interest are the two peaks and the trough that occur

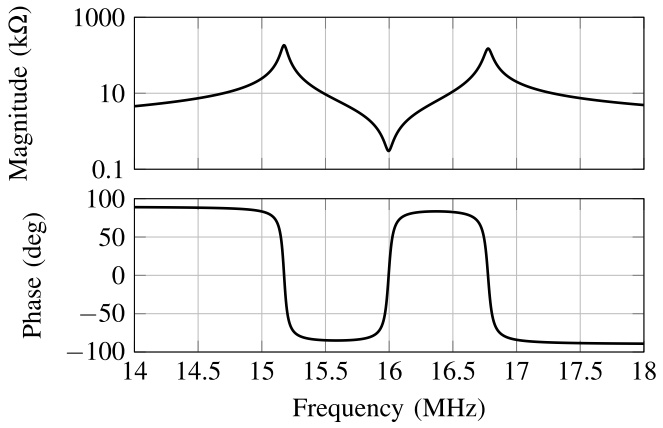


Fig. 4. Impedance plots for a symmetric link. $L_{1,2} = 10\ \mu$H, $C_{1,2} = 10$ pF, $M = 1\ \mu$H, $R_{1,2} = 3\ \Omega$.

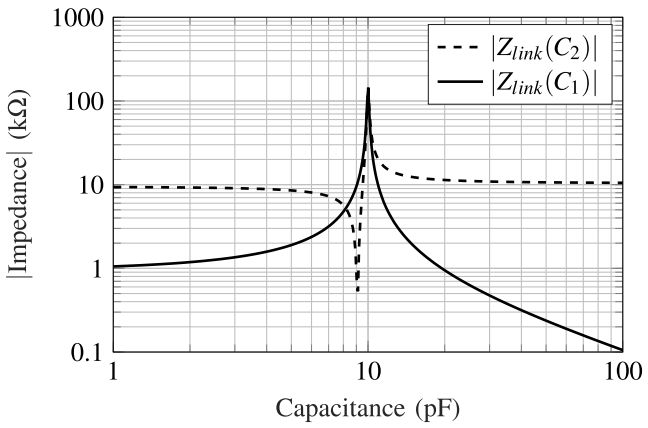


Fig. 5. Magnitude of the link impedance for varying values of $C_{1,2}$.

in the magnitude plot. These points will be referred to as the resonance and anti-resonance points respectively, and occur at corresponding resonance and anti-resonance frequencies.

Since the resonance and anti-resonance points are local maxima and minima in the function $|Z_{link}(\omega)| = \sqrt{\Re\mathrm{e}\{Z_{link}\} + \Im\mathrm{m}\{Z_{link}\}}$, they can be determined by partial differentiation:

$$\frac{\partial\{|Z_{link}(\omega)|\}}{\partial\omega} = 0. \tag{3}$$

By solving (3), the resonance ($\omega_{\text{res}(1,2)}$) and anti-resonance ($\omega_{\text{antires}}$) frequencies can be determined. The solution of (3) results in a 12th order polynomial, that is readily solvable numerically. If $M$ is low enough that the link is undercoupled, there will be one positive real root corresponding to a single value for $\omega_{\text{res}(1)}$. If $M$ is high enough that the link is overcoupled, there will be three positive real roots: $\omega_{\text{res}(1)} < \omega_{\text{antires}} < \omega_{\text{res}(2)}$. The exact boundary between the undercoupled and overcoupled conditions is defined by the critical coupling $k_{crit}$ [20]:

$$k_{crit} = \frac{1}{\sqrt{Q_1 Q_2}} \tag{4a}$$

$$\therefore M_{crit} = k_{crit}\sqrt{L_1 L_2}. \tag{4b}$$

For $k < k_{crit}$, the link is undercoupled, and for $k > k_{crit}$, the link is overcoupled.

It is possible to characterize the link in a similar way with respect to the capacitances $C_1$ and $C_2$, and observe how they are related to $\omega_{\text{res}(1,2)}$ and $\omega_{antires}$. The link impedance can be considered a function of either $C_1$ or $C_2$: ($\left|Z_{link}(C_{1,2})\right|$), and by substituting a known resonance frequency $\omega_{\text{res}(1,2)}$, the link can be characterized in terms of $C_1$ or $C_2$.

Fig. 5 shows $|Z_{link}|$ for the same link as in Fig. 4, where $\omega = \omega_{\text{res}(2)} = 16.78$ MHz. The key feature of the plots in Fig. 5 is that the curve of $|Z_{link}(C_1)|$ shows a single resonance point, and $|Z_{link}(C_2)|$ shows a resonance point and an anti-resonance point. By differentiation of $|Z_{link}|$ but with respect to $C_1$ or $C_2$, either capacitance can be determined, provided the other link parameters and the operating frequency $\omega$ is known. Solving

$$\frac{\partial\{|Z_{link}(\omega)|\}}{\partial C_1} = 0 \tag{5}$$

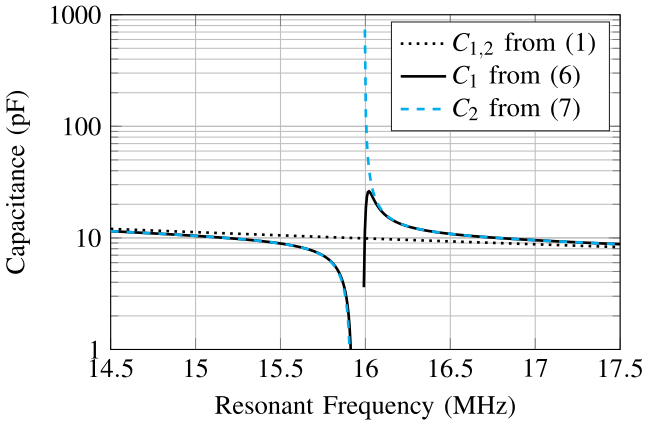


Fig. 6. Determining capacitance through resonant frequency.

results in a closed form expression for $C_1$, shown in (7), as shown at the bottom of the next page. Similarly, solving:

$$\frac{\partial\{|Z_{link}(\omega)|\}}{\partial C_2} = 0 \tag{6}$$

results in two closed form expressions for $C_2$, corresponding to the resonance and anti-resonance points. The solution for the resonance point is relevant here, and is given in (8), as shown at the bottom of the next page.

Therefore, if either $C_1$ or $C_2$ has an unknown value, the link is known to be resonating, and all the other link parameters are known, the unknown capacitance can be determined using either (7) or (8) respectively. To solve (5) and (6) and generate (7) and (8), the symbolic solver in SageMath was used, using the online CoCalc service [21].

Fig. 6 shows the results of determining unknown capacitances $C_1$ or $C_2$, across a range of resonant frequencies, where all other parameters are the same as those used in Fig. 4. For comparison, the solution according to (1) has been added. This highlights the error that arises by using (1); in particular where the resonant frequency is between 15.5 MHz and 16.5 MHz (i.e. the change in capacitance is small), the error between the two approaches becomes very significant; (1) is no longer a suitable approximation. Note that (7) and (8) have an asymptote with no solutions near the initial anti-resonance

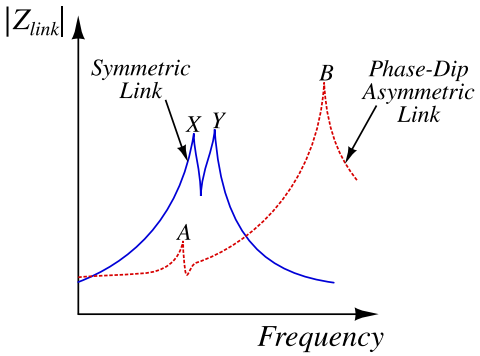


Fig. 7. Symmetric vs asymmetric link impedances, resonance points marked.

frequency of the link (see Fig. 4). This is because, given the other link parameters, there is no capacitance value for $C_1$ or $C_2$ that could allow link resonance in this frequency range.

### C. Self-Oscillation

The key advantage of the analysis presented in Section II-B is that an unknown capacitance can be determined in an otherwise characterised resonating link with arbitrary characteristics; there is no requirement to have $L_1 \ll L_2$ as in the phase-dip method. Given that resonance is a requirement, a self-oscillating circuit can be employed in order to perform the measurement, in combination with a frequency counter. This is a much simpler solution than the impedance analyzer required for a phase-dip measurement. Fig. 7 illustrates the qualitative difference in $|Z_{link}|$ for the asymmetric link used in the phase-dip method and a symmetric link. In the case of a self-oscillating circuit, a large resonance point impedance is required to maintain oscillation. In the asymmetric link, a self-oscillating circuit will oscillate at the higher-frequency peak, influenced mostly by the combination of $L_1$ and the negligible parasitic $C_{stray}$ ($C_1$). While it is possible to use (8) to determine the value of $C_{SENS}$, the sensitivity will be extremely poor. It is for this reason that the lower frequency

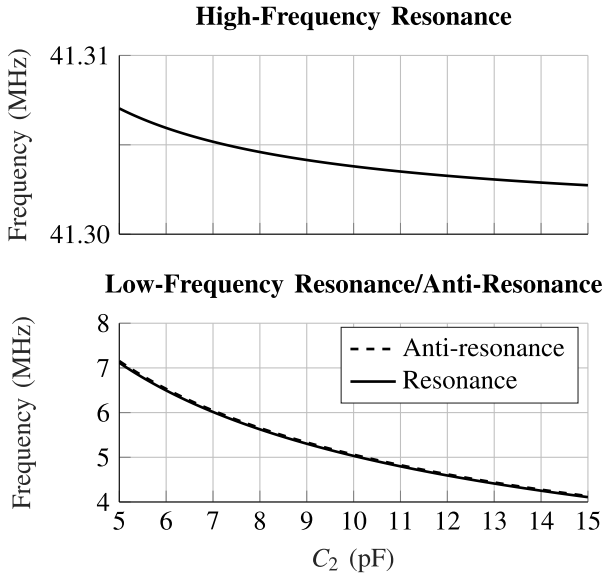


Fig. 8. Lines of resonance and anti-resonance for an asymmetric link as $C_2$ is swept. Parameters are the same as in Fig. 2 except $C_{stray} = 1.5$ pF.

peak (influenced mostly by the combination of $L_2$ and $C_{SENS}$) is used in the phase-dip method. In the case of the symmetric link however, both peaks are similarly affected by changes in capacitance at either $C_1$ or $C_2$. Therefore, regardless of which resonant peak the self-oscillator locks to, poor sensitivity is not an issue.

This difference in sensitivity is highlighted in Figs. 8 and 9, where the resonance points (marked X,Y for the symmetric link and A,B for the asymmetric link in Fig. 7) are plotted against changes in $C_2$. Fig. 8 is split into two parts to highlight the full dynamic ranges of the low and high frequency lines. For the range of 5 pF $< C_2 <$ 15 pF, the high frequency line in Fig. 8 shows a dynamic range of less than 10 kHz, whereas the low frequency line shows a dynamic range of approximately 3 MHz. In the symmetric link case as shown in Fig. 9, it can be seen that both the high and low frequency lines

$$C_1 = \frac{(C_2^2L_1L_2^2 - C_2^2L_2M^2)\omega^4 + (C_2^2L_1R_2^2 - 2C_2L_1L_2 + C_2M^2)\omega^2 + L_1}{(C_2^2L_1^2L_2^2 - 2C_2^2L_1L_2M^2 + C_2^2M^4)\omega^6 + (C_2^2L_2^2R_1^2 + 2C_2^2M^2R_1R_2 + C_2^2L_1^2R_2^2 - 2C_2L_1^2L_2 + 2C_2L_1M^2)\omega^4 + (C_2^2R_1^2R_2^2 - 2C_2L_2R_1^2 + L_1^2)\omega^2 + R_1^2} \tag{7}$$

$$\begin{aligned}
C_2 &= \frac{A + \sqrt{B}}{C} \\
A &= 2\left(C_1L_1^2L_2 - C_1L_1M^2\right)\omega^4 - \left(2\,C_1L_2R_1^2 + 4\,C_1L_1R_1R_2 + 2\,L_1L_2 - M^2\right)\omega^2 + 2\,R_1R_2 \\
B &= 4\left(C_1^2M^4R_1^2 + 2\,C_1^2L_1^2M^2R_1R_2 + C_1^2L_1^4R_2^2\right)\omega^6 + \left(M^4 + 8\left(C_1^2L_1^2R_1^2 - C_1L_1^3\right)R_2^2 + 8\left(C_1^2M^2R_1^3 - C_1L_1M^2R_1\right)R_2\right)\omega^4 \\
&\quad +4\,R_1^2R_2^2 + 4\left(M^2R_1R_2 + \left(C_1^2R_1^4 - 2\,C_1L_1R_1^2 + L_1^2\right)R_2^2\right)\omega^2 \\
C &= 2\,(\left(C_1L_1^2L_2^2 - 2\,C_1L_1L_2M^2 + C_1M^4\right)\omega^6 - \left(C_1L_2^2R_1^2 + C_1L_1^2R_2^2 + L_1L_2^2 - L_2M^2 + 2\left(2\,C_1L_1L_2 - C_1M^2\right)R_1R_2\right)\omega^4 \\
&\quad +\left(2\,L_2R_1R_2 + \left(C_1R_1^2 + L_1\right)R_2^2\right)\omega^2)
\end{aligned} \tag{8}$$

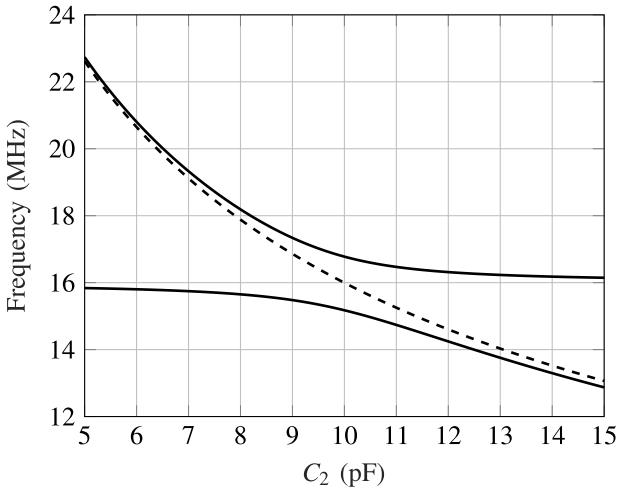


Fig. 9. Lines of resonance and anti-resonance for a symmetric link as $C_2$ is swept. Parameters the same as in Fig. 4.

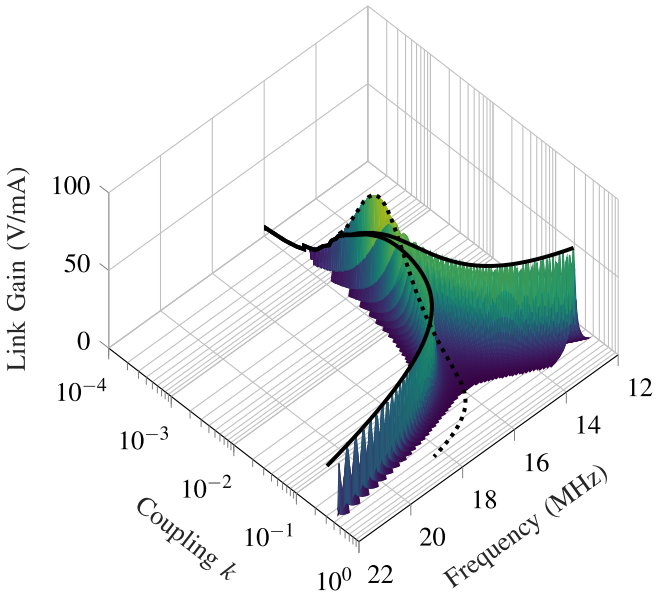


Fig. 10. Link gain vs coupling and frequency. Lines of resonance and anti-resonance are highlighted.

of resonance show a large dynamic range of approximately 7 MHz and 3 MHz respectively. Whether the oscillator locks to the higher or lower frequency resonance point for a given capacitance is not a concern; there is no point at which the resonance lines can overlap and cause an ambiguous solution.

### *D. Link Coupling*

The previous analysis has assumed a fixed mutual inductance $M$ between the two coils, without considering how the value of $M$ affects the link performance. In the active mode, variations in $M$ affect the amplitude of the signal at the receiver, whereas in the passive mode variations in $M$ primarily affect the sensitivity to changes in $C_{SENS}$. In both cases variations in $M$ can cause measurement errors, since (7) and (8) both depend on $M$ as well as $\omega$, changes in $M$ can be misinterpreted as changes in $C_{SENS}$.

Link coupling is considered in terms of the unitless coupling coefficient $k$ rather than mutual inductance $M$ in some of this section, where:

$$k = M/\sqrt{L_1 L_2} \tag{9}$$

$k = 1$ indicates perfect coupling between $L_1$ and $L_2$ and $k = 0$ indicates that $L_1$ and $L_2$ are entirely uncoupled.

*1) Active Mode:* In the active mode, the coupling is the principal factor determining the amplitude of the signal at the receiver. As the coupling decreases, the gain also decreases. For the circuit in Fig. 3, following the procedure defined in [20], the link gain is defined as:

$$\frac{V_{out}}{I_{in}} = \frac{-j\omega M \left(j\omega C_1 + \frac{1}{R_1 + j\omega L_1 + Z_{refl}}\right)^{-1}}{\left(R_1 + j\omega L_1 + Z_{refl}\right)\left(R_2 + j\omega L_2 + \frac{1}{j\omega C_2}\right) j\omega C_2} \tag{10}$$

where $V_{out}$ is the voltage across the capacitor $C_2$, $I_{in}$ is a constant ac input current with frequency $\omega$ in parallel with the input at $C_1$, and $Z_{refl}$ is the impedance reflected from the secondary to the primary, where:

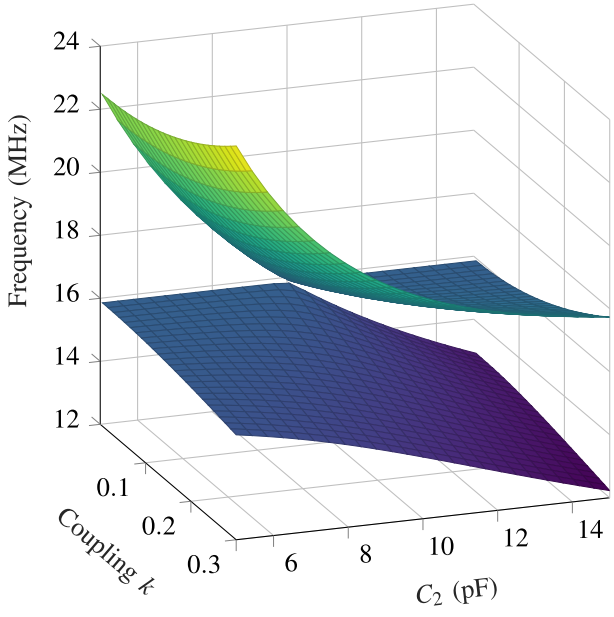


Fig. 11. Planes of resonance against changes in $C_2$ and $k$.

$$Z_{refl} = \frac{\omega^2 M^2}{R_2 + j\omega L_2 + \frac{1}{j\omega C_2}}. \tag{11}$$

Equation (10) shows how the link gain depends significantly on $M$. Fig. 10 shows a plot of (10) using the example values from Fig. 4, sweeping coupling and frequency. The lines of resonance/anti-resonance are mapped onto the surface; as long as the coupling stays sufficiently high ($k \geq 0.005$ in this case) the gain stays maximized.

This analysis assumes a high impedance at the frequency counter input, hence the gain remaining high over a wide range

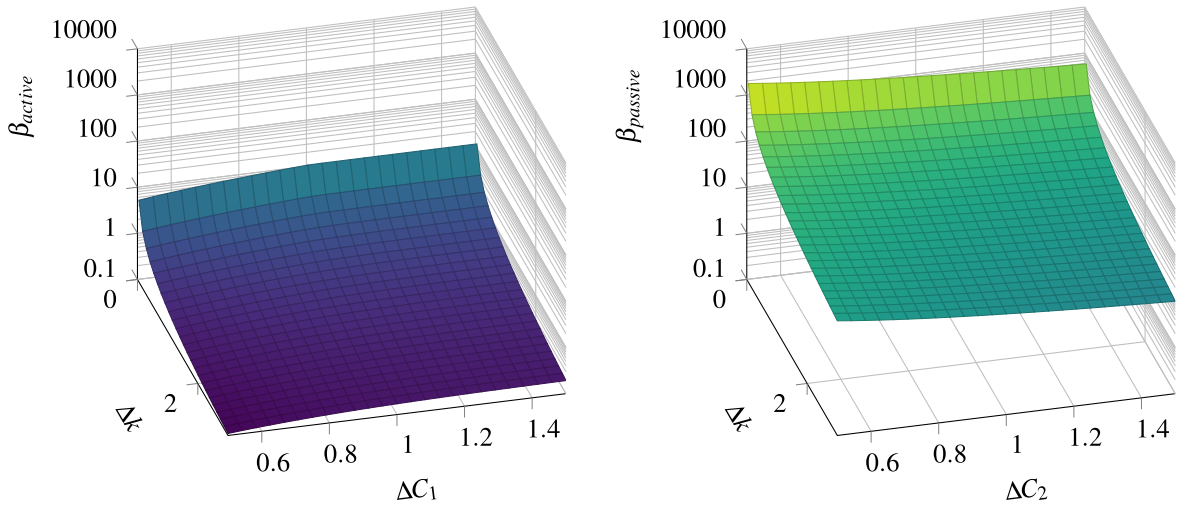


Fig. 12. Plots of (a) $\beta_{active}$ and (b) $\beta_{passive}$ against variations in $\Delta k$ and $\Delta C_{(1,2)}$. Nominal parameters again are the same as in Fig. 4, $k_{(nom)} = 0.1$, $C_{(1,2)_{(nom)}} = 10$ pF.

of couplings. Further resistive loading across $C_2$ will reduce this gain particularly at lower couplings.

*2) Passive Mode:* In the passive mode, the coupling significantly affects the dynamic range (in Hz/F). Fig. 11 shows the results of (8) plotted against both $k$ and $C_2$. Fig. 11 demonstrates that, at low couplings, the resonance lines that lie furthest from the anti-resonance plane show an almost flat response compared with those at high couplings. While the resonance planes still show a wide dynamic range for the regions near the anti-resonance plane, the value of $|Z_{link}|$ for these points will be low (cf. the asymmetric plot in Fig. 7). As a result, the oscillator will not oscillate in these regions, only in the flattened regions far from the anti-resonance plane.

*3) Errors Due to $\Delta k$:* The aim of (7) and (8), is to convert a measured $\Delta\omega$ to $\Delta C$. However, $\Delta M$ will also correlate to a measured $\Delta\omega$.

To determine an ideal region of operation, the relative impacts of $\Delta C_{(1,2)}$ and $\Delta M$ on $\Delta\omega$ should be considered. First, the $\Delta$ quantities are defined as follows:

$$\Delta C_1 = C_1/C_{1_{(nom)}} \tag{12a}$$
$$\Delta C_2 = C_2/C_{2_{(nom)}} \tag{12b}$$
$$\Delta M = M/M_{(nom)} \tag{12c}$$

where $(nom)$ denotes the nominal value. Equation (12) defines the $\Delta$ quantities as unitless proportional deviations from the norm, and thus $\Delta C$ and $\Delta M$ can be directly compared.

The relation in (3) effectively provides a function that describes how changes in $|Z_{link}|$ parameters are converted to changes in $\omega$. The positive real roots of this function for varying $Z_{link}$ parameters can be considered as functions $\gamma_n(Z_{link})$, where $n$ is the root number, and $n \geq 1, n \in \mathbb{R}$. Odd positive root numbers define resonance points, even root numbers define antiresonances. Here the resonance points are of interest, so from here $\gamma = \gamma_1$. Using partial differentiation, the sensitivity of $\gamma$ to $\Delta C_{(1,2)}$ and $\Delta M$ can be determined. The relative sensitivities of $\gamma$ to $M$ and $C_{(1,2)}$ can be expressed as ratios:

$$\beta_{active} = \left(\frac{\partial\gamma}{\partial\Delta C_1}\right) \Big/ \left(\frac{\partial\gamma}{\partial\Delta M}\right) \tag{13}$$
$$\beta_{passive} = \left(\frac{\partial\gamma}{\partial\Delta C_2}\right) \Big/ \left(\frac{\partial\gamma}{\partial\Delta M}\right). \tag{14}$$

Equations (13) and (14) provide ratios for the sensitivity of $\omega$ to $\Delta C_{SENS}/\Delta M$ for the active ($\beta_{active}$) and passive ($\beta_{passive}$) modes respectively.

To minimize the effect of $\Delta M$ on the measured value of $\Delta\omega$, the link should be far more sensitive to changes in capacitance than coupling, i.e. $\beta_{active}$ and $\beta_{passive}$ should both be large.

Fig. 12 shows planes of $\beta_{active}$ and $\beta_{passive}$ for sweeps of $k$ and $C_{SENS}$. A notable difference is that the value of $\beta_{active}$ is up to $1000\times$ smaller than the value of $\beta_{passive}$. This indicates that in the active mode, the measurement is far more susceptible to errors due to $\Delta k$ than in the passive mode. For example, the worst case $\beta_{active}$ in Fig. 12(a) is $\approx 0.1$, indicating that the output frequency for this point is $\approx 10\times$ more sensitive to $\Delta k$ than it is to $\Delta C_1$, whereas for $\beta_{passive}$ the minimum value is $\approx 10$. Both planes however share the trend that $\beta$ improves as the coupling decreases; both curves show an improvement of two orders of magnitude as $k$ is swept from 0.3 to 0.005. This reduction in coupling is at the cost of gain or dynamic range for the active and passive case respectively.

For the active case, the coupling should be minimized to minimize the error due to $\Delta k$, limited by ensuring the link gain is still sufficient for detection at the counter. In the passive case, again coupling should be minimized, but in this case limited by ensuring dynamic range is sufficient (see Fig. 11).

### *E. Series Losses*

Section II-B provides an exact method for determining an unknown capacitance from the frequency of an otherwise

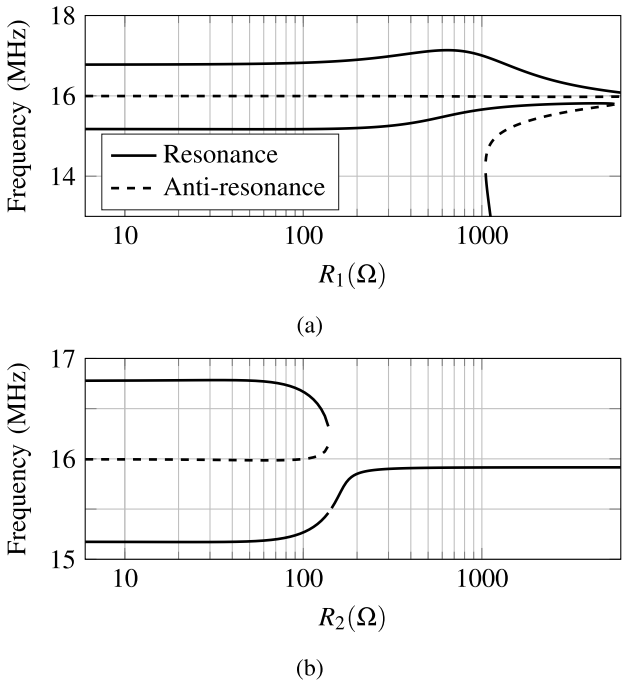


Fig. 13. Lines of resonance and anti-resonance against changes in $R_1$ and $R_2$. Other link parameters the same as in Fig. 4.

characterized resonating link. However, errors can occur if there is a change in series loss ($R_1$ or $R_2$) in addition to a change in $C_{SENS}$. This is a valid concern given that, depending on the sensing method and substance being sensed, a capacitive sensor may present a significant series loss compared to solid dielectrics or free space [22]–[24].

If the capacitive series loss resistance is large enough, it has a significant effect on the resonant frequency and would effectively stop an accurate measurement of capacitance from (7) or (8). The frequency change would be due to a change in both $C_{SENS}$ and $R_1$ or $R_2$. This effect is illustrated in Fig. 13, where (3) is solved against varying values of $R_1$ and $R_2$. As long as $R_1$ and $R_2$ remain below 100 Ω, the lines of resonance/antiresonance remain largely unaffected; they remain constant at the same frequencies as shown in Fig. 4. However for larger values of series loss ($\geq$ 100 Ω or so in this example), these lines suffer significant shifts. Therefore if a test substance introduces significant loss in addition to a change in capacitance, the capacitance change can no longer be reliably determined by using (7) or (8).

The effect of series losses can be considered somewhat similarly to the issues arising from coupling variations. However there is no tradeoff in this case; ideally the loss should always be minimized to preserve the accuracy of the $C_{SENS}$ measurement.

The preceding series loss analysis assumes that series loss in the capacitors $C_{1,2}$ can be lumped into the series loss of the coils, and simply added to $R_{1,2}$. It should be noted that this assumption is only valid for the link arrangement used here, a parallel-parallel link with a current-mode driver and a high (near infinite) load resistance.

Fig. 14 shows a more detailed link diagram that includes the series loss resistance of both $C_{1,2}$ and $L_{1,2}$. If $I_{in}$ has a very high output impedance, and $R_{out}$ is also very large, then the $R_C$ and $R_L$ elements can be considered as singular combined losses $R_{1,2}$, as in Fig. 3.

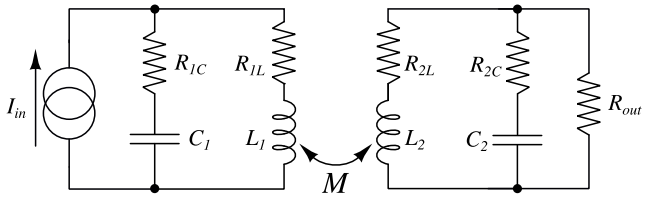


Fig. 14. More detailed link diagram, including series loss in capacitors.

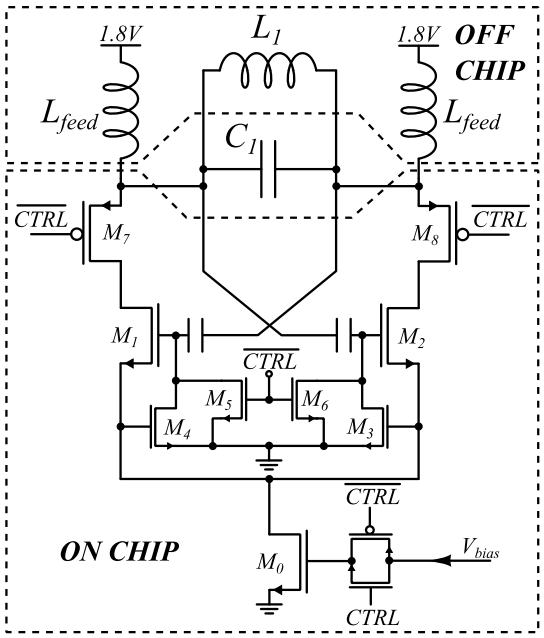


| | |
|---|---|
| $M_0$ | 200$\mu$/5$\mu$ |
| $M_{1,2}$ | 72$\mu$/1$\mu$ |
| $M_{3,4}$ | 220n/10$\mu$ |
| $M_{5,6}$ | 2$\mu$/350n |
| $M_{7,8}$ | 2048$\mu$/300n |

Fig. 15. *Top*: Cross-coupled oscillator circuit. $C_1$ is on or off chip depending on active or passive configuration. *Bottom*: Table of device dimensions.

## III. Circuit Design

### A. Oscillator Circuit

In order to test the method of measurement; a self-oscillating circuit, shown in Fig. 15, was designed in 0.18 $\mu$m CMOS. It is a cross-coupled design, fed by a current source at its tail to control amplitude of oscillation.

The oscillator is controlled by complementary control signals *CTRL* and $\overline{CTRL}$. When *CTRL* goes high, the switches $M_{7,8}$ are turned on, connecting the oscillator to the transmission coil, and the transmission gate feeding $M_0$ is opened to allow bias current control. When *CTRL* goes low, $M_{5,6}$ turn on to force the gates of $M_{1,2}$ low and damp any oscillation during turnoff. $M_{3,4}$ are long devices arranged to behave as a gate bias mechanism; these devices complement the fact

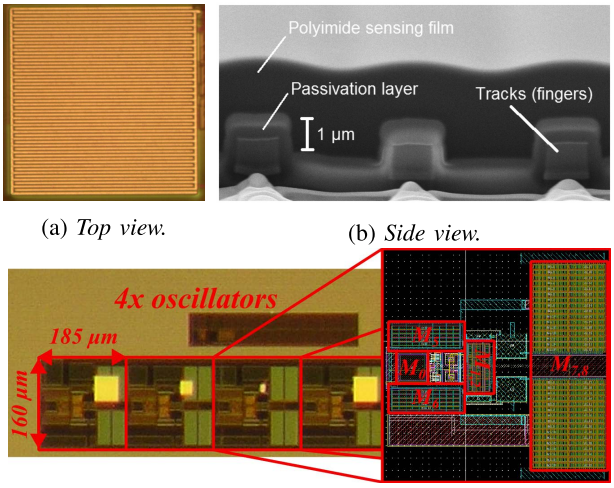


(a) *Top view.* (b) *Side view.*

(c) *Chip photo, circuit elements highlighted.*

Fig. 16. Microscope (a) and ion-beam (b) images of the humidity sensing capacitor. (c) shows a close-up image of the fabricated circuits and their area, layout detail is highlighted.

that $M_{1,2}$ are 'native' enhancement mode NMOS devices, with $V_T \approx 0$ V. When the oscillator is on, the voltage at the drain of $M_0$ will always be a few mV above ground, this small voltage is enough to maintain $M_{3,4}$ in the subthreshold region, where they present a large pseudoresistance from gate to ground for $M_{1,2}$. $M_{3,4}$ also act in a loop to prevent the DC level of the gate voltages of $M_{1,2}$ from rising over time. This action can be considered as follows: if the gate voltage at $M_1$ rises slightly, the source voltage should also rise slightly, as $M_0$ will still be providing the same bias current. This slight rise in source voltage will reduce the resistance provided by $M_4$, bringing the gate voltage at $M_1$ back down. Since $M_{3,4}$ are long channel and operating in subthreshold, they do not respond to rapid changes at oscillation frequency, only to quasi-static drifts.

Fig. 16(c) shows a photo of the fabricated chip, with 4 independent oscillator circuits visible, each occupying an area of 160 $\mu m$ × 185 $\mu m$. An enlarged layout image is inset, highlighting the relative size of the key structures.

### *B. Humidity Sensing Capacitors*

As an example capacitive sensing element, an on-chip CMOS humidity sensing capacitor was used [25], its structure is illustrated in Figs. 16(a) and 16(b). The capacitor consists of interdigitated top metal fingers, with a polyimide film on the surface above the passivation. As the polyimide absorbs humidity from the environment, its dielectric constant changes, altering the capacitance. These on-chip capacitors were confirmed to have low series losses ($< 1\ \Omega$), and as such comply with the requirement for a low series loss sensing element as previously explained in Section II-E.

The nominal capacitance of these capacitors is dependent on frequency, particularly at higher humidities [26], [27]. Here the capacitive variability is significantly reduced for frequencies beyond 1 MHz. In this work, the operating frequency is always higher than 10 MHz, therefore the capacitive dependence on frequency can be neglected.

TABLE I
MEASURED NOMINAL LINK PARAMETERS

| *Common* | | *Active* | | *Passive* | |
|---|---|---|---|---|---|
| $L_{1,2}$ | 7.34 $\mu$H | $C_1$ | 13.4 pF | $C_1$ | 18.7 pF |
| $R_{1,2}$ | 6.0 $\Omega^{\dagger}$ | $C_2$ | 19.5 pF | $C_2$ | 7.5 pF |
| $k$ | 0.217 | $\beta$* | 0.588 | $\beta$* | 1.950 |

$^{\dagger}$Measured coil loss, $C_{SENS}$ series loss is neglected here.

*$\beta$ values calculated from measured link parameters.

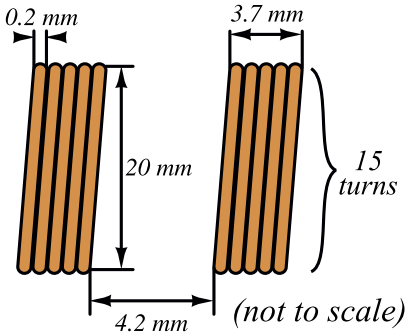


Fig. 17. Nominal geometric specifications of the fabricated link coils. Both coils are circular, identical, and coaxially aligned.

## IV. MEASURED RESULTS

The system was tested in both the active and passive sensor configurations in order to determine the effectiveness of the method. The system was arranged as shown in Fig. 18, and the nominal link parameters were measured. These link parameters are summarized in Table I, as well as predicted values for $\beta_{active}$ and $\beta_{passive}$. The link coils were single layer solenoids constructed from standard enamelled magnet wire, the details of their geometry are given in Fig. 17. Most of the tests were conducted at a distance of 4.2 mm ($k = 0.217$), to obtain good dynamic range. Tests were also performed with 16.3 mm coil separation ($k = 0.056$); these are discussed later in this section.

In the active mode, the bulk of $C_2$ is formed by a 15 pF ceramic capacitor, the remaining capacitance comes from the parasitic capacitance of $L_2$ and the probe capacitances. $C_1$ is formed by $C_{SENS}$ and parasitics at the oscillator. In the passive mode, $C_1$ consists of parasitics at the oscillator and the probe capacitances. $C_2$ is formed by $C_{SENS}$ in addition to the parasitic capacitance of $L_2$.

In both cases, the parasitic capacitance at the oscillator is relevant; it is important therefore to maintain a constant bias current in the oscillator circuit, since the parasitic capacitance will depend on this bias. The correlation between bias and oscillation frequency is described in [28]; for the purposes of this work, increasing $V_{bias}$ approximately generates an increasing shunt capacitance $C_{shunt}$ that appears in parallel with the LC tank. By maintaining $V_{bias}$ at a constant value, $C_{shunt}$ will stay constant also.

Tests were performed in a climate controlled chamber (Binder KMF 115), for a range of humidities (20-90 %rh). The chamber was left to settle for 5 minutes after each change

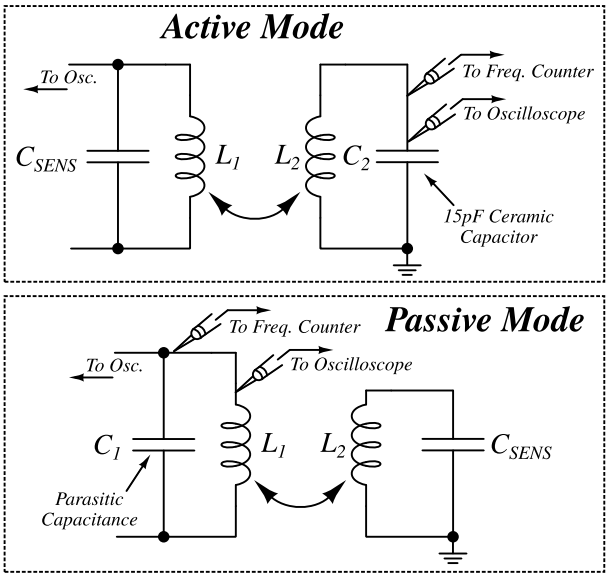


Fig. 18. Test arrangements for the active and passive modes.

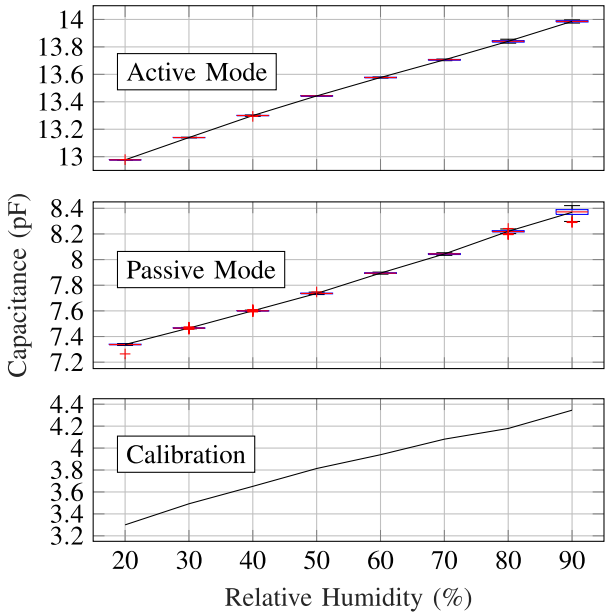


Fig. 19. Raw relative humidity data from the system in active and passive mode, compared with calibration data from the capacitive sensor.

in humidity, and then 1000 samples were collected from the frequency counter (HP 53131A). The temperature was fixed at 35 °C.

Fig. 19 shows measured data for the results of testing the system in active and passive mode, and a calibration plot, where the capacitor was measured by an impedance analyzer. The active mode and passive mode plots show that the same change in capacitance can be detected in both configurations, and matches well with the calibration plot. The error bars for the plots in Fig. 19 are boxplots of the real data gathered from the counter. The boxplots show very little variation, with the maximum measured standard deviation occurring at 90% humidity in passive mode, where $\sigma = 28$ fF.

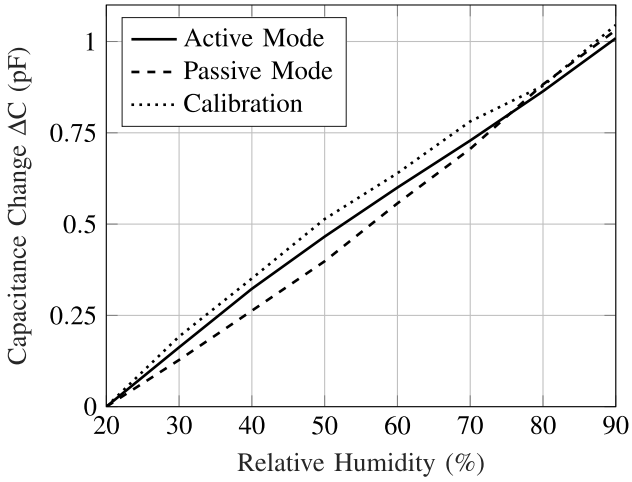


Fig. 20. Capacitive deviation as a function of relative humidity for the active and passive modes.

TABLE II
SUMMARY OF CORRELATION AND ERROR BETWEEN SYSTEM MEASUREMENTS AND CALIBRATION MEASUREMENTS

| | *Absolute Error (pF)* | *r Value* |
|---|---|---|
| *Active Mode* | $\mu = 0.0311$ $\sigma = 0.0172$ | 0.9991 |
| *Passive Mode* | $\mu = 0.0555$ $\sigma = 0.0437$ | 0.9925 |

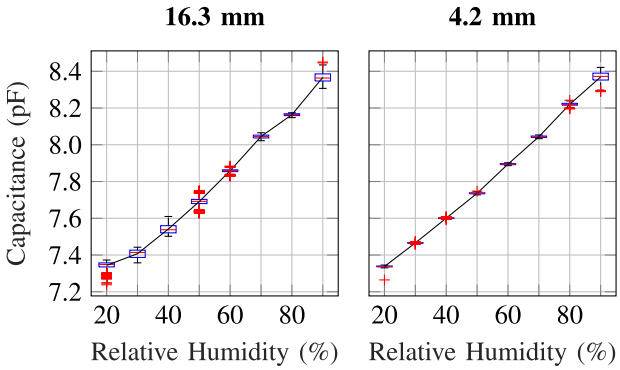


Fig. 21. Passive mode capacitance measurements for different coil spacings.

The main sources of error in this experiment are the stability of the humidity chamber itself and the phase noise of the oscillator, which is seen as capacitive measurement noise after being converted by (7) or (8). The worst case $\sigma$ of 28 fF at 90 %rh in passive mode suggests a minimum resolvable relative humidity step of $< 2$ %rh. Given that the specified humidity fluctuation of the chamber is $\leq 2.5$ %rh, it is possible that this variance is due to the chamber rather than the circuit.

Fig. 20 shows the relative measured capacitive change for the active and passive modes compared to the impedance analyzer measurement. The worst case difference is an error of 0.1 pF between the passive mode and the calibration plot occurring at 50 %rh.

Table II summarizes the absolute errors (mean and standard deviation) and correlation coefficients for the active and passive mode results, compared with those from the calibration

TABLE III
COMPARISON WITH OTHER RECENT WIRELESS SENSING SYSTEMS

| Parameter | **This Work** | Ahmadi et. al. 2009 [3] | Lee et. al. 2016 [7] | Zhang et. al. 2015 [8] |
|---|---|---|---|---|
| Size | Miniature | Miniature | Benchtop | Benchtop |
| Power | Low ($72\ \mu\text{W} - 1.44$ mW$^{\dagger}$) | Low ($198\ \mu\text{W}^{\dagger\dagger}$) | High | High |
| Complexity | Low | High | Moderate | Moderate |
| Method | Direct $C$ to $f$ Conversion and FM Wireless Transmission | Glucose to Current Conversion, A2D Encoding, and Digital Wireless Transmission | Frequency Sweep Impedance Interrogation | Frequency Sweep Impedance Interrogation |
| Active/Passive | Active or Passive | Active* Only | Passive Only | Passive Only |
| Sensitivity | Passive: 635 Hz/%rh, Active: 1.188 kHz/%rh | $1.25 - 8.8$ nA/mM | 304 kHz/kPa | 18.71 kHz/%rh |
| Frequency Range | $12 - 14$ MHz | DC Sensing, 13.56 MHz RF Carrier | $160 - 170$ MHz | $35 - 37$ MHz |
| Operating Distance (Max) | 16.3 mm | 4 cm | 20 mm | 5 mm |

$^{\dagger}$Not including frequency counter.
$^{\dagger\dagger}$Not including RF transmitter.
*While the modulation scheme is technically 'passive' (load-shift keying), the direction is one way from the remote side to the local side; this is therefore comparable to the active mode in this work.

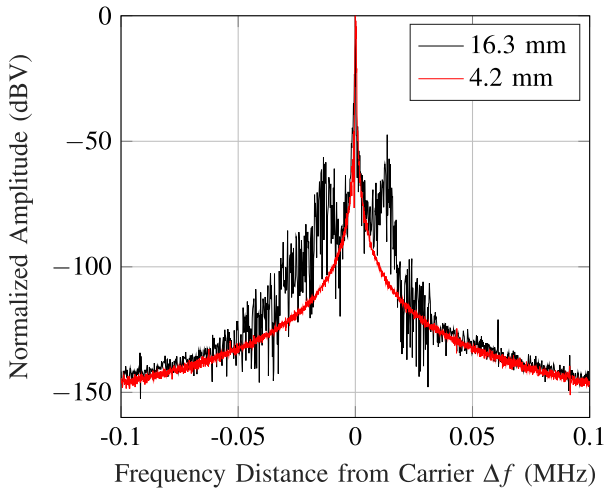


Fig. 22. Output spectra for different coil spacings.

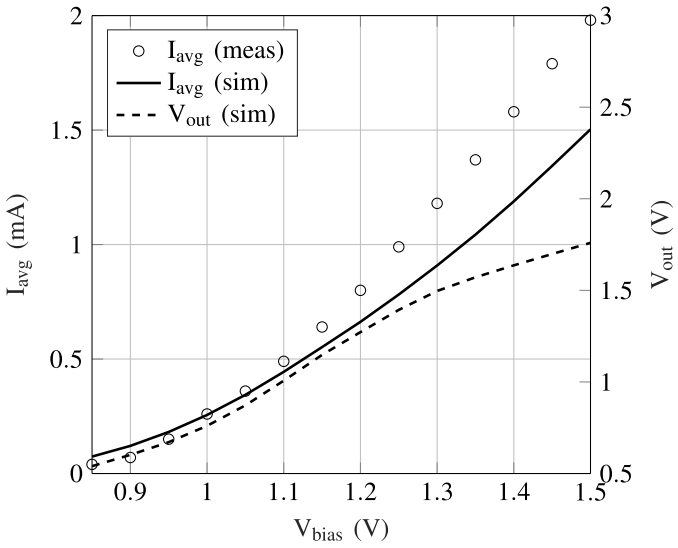


Fig. 23. Measured and simulated average current consumption ($I_{avg}$) and oscillator output amplitude ($V_{out}$) as $V_{bias}$ is varied.

run (based on the data in Fig. 20). These statistical results from the system show good correlation with the calibration run; the worst case mean absolute error of 55.5 fF correlates to a humidity sensing error of 3.9 %rh, with respect to the calibration run with the impedance analyzer.

### A. Reduced Coupling

To assess the effect of reducing the coupling on system performance, the distance between the coils was increased from 4.2 mm to 16.3 mm, and the system was tested in passive mode. Fig. 21 shows measured capacitance against humidity for 4.2 mm and 16.3 mm coil spacings. While the overall trend remains the same, as the distance is increased the accuracy is reduced. This is shown by the boxplots for each humidity value having larger spreads than those from the shorter range tests.

The reason for this increased spread in the results can be explained by increased phase noise in the oscillator as the distance between the coils is increased. This is illustrated in Fig. 22. This increase in frequency variability directly translates to an increase in measurement variability, increasing the overall uncertainty. It is therefore important to consider the effect of coil coupling on the phase noise of the oscillator, as it has a direct impact on the measurement accuracy.

### B. Power Consumption

The total current consumption of the circuit was also measured, and compared with the average current consumption in postlayout simulation. Since the consumption of the system is strongly dependent on $V_{bias}$, it was measured for a range of $V_{bias}$ values.

Fig. 23 shows the average current consumption of the circuit from a 1.8 V supply as $V_{bias}$ is varied from 0.85 V to 1.5 V,

and the peak to peak voltage output at the oscillator. The curves show that the output starts compressing at $V_{bias} > 1.2$ V; the bias was therefore fixed here to maximize the output without wasting power in distortion. The measured current consumption for $V_{bias} = 1.2$ V was 0.8 mA, or 1.44 mW total power dissipation. The minimum power dissipation at $V_{bias} = 0.85$ V is 72 $\mu$W.

## V. Conclusion

This paper has presented a method for performing near-field wireless sensing of a capacitive sensing element, requiring only a self-oscillating circuit and a frequency counter. The developed theory has been verified through circuit fabrication and experiment, with the results suggesting good accuracy. Compared with the current state of the art, this approach bridges the gap between miniaturized wireless measurement systems, that require complex signal processing chains, and direct inductive link based measurement systems, that require benchtop impedance analyzers.

A comparison with the state of the art is provided in Table III. The key elements to note are that the method presented in this work is suitable for miniaturized implementations at low power consumptions, without the associated complexity that otherwise is required. In addition, the method is reversible; the same fundamental circuits are used for both active and passive modes.

Given that the method presented in this work is flexible and low complexity, and the circuits are miniaturizable and low power, they would be well placed in a variety of fast-growing wireless sensing applications, for example in the biomedical, food quality, and environmental monitoring domains.

## References


[1] Y. Zhang *et al.*, "A batteryless 19 $\mu$W MICS/ISM-band energy harvesting body sensor node SoC for ExG applications," *IEEE J. Solid-State Circuits*, vol. 48, no. 1, pp. 199–213, Jan. 2013.

[2] N. J. Cleven *et al.*, "A novel fully implantable wireless sensor system for monitoring hypertension patients," *IEEE Trans. Biomed. Eng.*, vol. 59, no. 12, pp. 3124–3130, Nov. 2012.

[3] M. M. Ahmadi and G. A. Jullien, "A wireless-implantable microsystem for continuous blood glucose monitoring," *IEEE Trans. Biomed. Circuits Syst.*, vol. 3, no. 3, pp. 169–180, Jun. 2009.

[4] Y.-J. Huang *et al.*, "A self-powered CMOS reconfigurable multi-sensor SoC for biomedical applications," *IEEE J. Solid-State Circuits*, vol. 49, no. 4, pp. 851–866, Apr. 2014.

[5] E. L. Tan, W. N. Ng, R. Y. Shao, B. D. Pereles, and K. G. Ong, "A wireless, passive sensor for quantifying packaged food quality," *Sensors*, vol. 7, pp. 1747–1756, Sep. 2007.

[6] K. G. Ong and C. A. Grimes, "A resonant printed-circuit sensor for remote query monitoring of environmental parameters," *Smart Mater. Struct.*, vol. 9, no. 4, p. 421, 2000.

[7] H. Y. Lee, B. Choi, S. Kim, S. J. Kim, W. J. Bae, and S. W. Kim, "Sensitivity-enhanced *LC* pressure sensor for wireless bladder pressure monitoring," *IEEE Sensors J.*, vol. 16, no. 12, pp. 4715–4724, Jun. 2016.

[8] C. Zhang, L.-F. Wang, J.-Q. Huang, and Q.-A. Huang, "An LC-type passive wireless humidity sensor system with portable telemetry unit," *J. Microelectromech. Syst.*, vol. 24, no. 3, pp. 575–581, Jun. 2015.

[9] N. T. Trung and P. Häfliger, "A submicrowatt implantable capacitive sensor system for biomedical applications," *IEEE Trans. Circuits Syst., II, Exp. Briefs*, vol. 62, no. 2, pp. 209–213, Feb. 2015.

[10] F. Chen, F. Lim, O. Abari, A. Chandrakasan, and V. Stojanovic, "Energy-aware design of compressed sensing systems for wireless sensors under performance and reliability constraints," *IEEE Trans. Circuits Syst. I, Reg. Papers*, vol. 60, no. 3, pp. 650–661, Mar. 2013.

[11] F. T. Lin, S. Y. Lu, and Y. T. Liao, "A 2.2 $\mu$Ws, −12 dbm RF-powered wireless current sensing readout interface ic with injection-locking clock generation," *IEEE Trans. Circuits Syst. I, Reg. Papers*, vol. 63, no. 7, pp. 950–959, Jul. 2016.

[12] J. V. Ham, I. E. Naert, and R. Puers, "Design and packaging of a fully autonomous medical monitoring system for dental applications," *IEEE Trans. Circuits Syst. I, Reg. Papers*, vol. 54, no. 1, pp. 200–208, Jan. 2007.

[13] M. H. Ghaed *et al.*, "Circuits for a cubic-millimeter energy-autonomous wireless intraocular pressure monitor," *IEEE Trans. Circuits Syst. I, Reg. Papers*, vol. 60, no. 12, pp. 3152–3162, Dec. 2013.

[14] F. Wang, X. Zhang, M. Shokoueinejad, B. J. Iskandar, J. E. Medow, and J. G. Webster, "A novel intracranial pressure readout circuit for passive wireless LC sensor," *IEEE Trans. Biomed. Circuits Syst.*, vol. 11, no. 5, pp. 1123–1132, Oct. 2017.

[15] M. Nowak, N. Delorme, F. Conseil, and G. Jacquemod, "A novel architecture for remote interrogation of wireless battery-free capacitive sensors," in *Proc. 13th IEEE Int. Conf. Electron., Circuits Syst.*, Dec. 2006, pp. 1236–1239.

[16] W. Q. Niu, J. X. Chu, W. Gu, and A. D. Shen, "Exact analysis of frequency splitting phenomena of contactless power transfer systems," *IEEE Trans. Circuits Syst. I, Reg. Papers*, vol. 60, no. 6, pp. 1670–1677, Jun. 2013.

[17] R. Huang, B. Zhang, D. Qiu, and Y. Zhang, "Frequency splitting phenomena of magnetic resonant coupling wireless power transfer," *IEEE Trans. Magn.*, vol. 50, no. 11, pp. 1–4, Nov. 2014.

[18] Y. Zhang, Z. Zhao, and K. Chen, "Frequency-splitting analysis of four-coil resonant wireless power transfer," *IEEE Trans. Ind. Appl.*, vol. 50, no. 4, pp. 2436–2445, Jul. 2014.

[19] M. Schormans, V. Valente, and A. Demosthenous, "Frequency splitting analysis and compensation method for inductive wireless powering of implantable biosensors," *Sensors*, vol. 16, no. 8, p. 1229, 2016.

[20] F. E. Terman, *Radio Engineers' Handbook*. New York, NY, USA: McGraw-Hill, 1943.

[21] *CoCalc—Collaborative Calculation in the Cloud*. Accessed: Dec. 10, 2017. [Online]. Available: https://cocalc.com

[22] R. Bartnikas, "Dielectric losses in solid-liquid insulating systems—Part I," *IEEE Trans. Elect. Insul.*, vol. TEI-5, no. 4, pp. 113–121, Dec. 1970.

[23] J. B. Whitehead, "Liquid insulators," *Trans. Electrochem. Soc.*, vol. 65, no. 1, pp. 35–46, 1934.

[24] C. G. Garton, "Dielectric loss in thin films of insulating liquids," *J. Inst. Elect. Eng., Part III, Commun. Eng., Including Process. Wireless Sec. Inst.*, vol. 88, no. 1, pp. 23–40, Mar. 1941.

[25] C. Eder, V. Valente, N. Donaldson, and A. Demosthenous, "A CMOS smart temperature and humidity sensor with combined readout," *Sensors*, vol. 14, no. 9, pp. 17192–17211, 2014.

[26] A. Tripathy *et al.*, "Design and development for capacitive humidity sensor applications of lead-free Ca,Mg,Fe,Ti-oxides-based electro-ceramics with improved sensing properties via physisorption," *Sensors*, vol. 16, no. 7, p. 1135, 2016.

[27] R. Akram, "Frequency dependence of electrical parameters of an organic-inorganic hybrid composite based humidity sensor," *Electronics*, vol. 5, no. 2, p. 23, 2016.

[28] J. Groszkowski, *Frequency of Self-Oscillations*. New York, NY, USA: Macmillan, 1964.


**Matthew Schormans** (S'14) received the M.Eng. degree in electronic and electrical engineering from University College London, London, U.K., in 2014, where he is currently pursuing the Ph.D. degree in electronic and electrical engineering, with a focus on short-range wireless power and data telemetry for implantable medical devices.

He has authored several conference and journal publications on biomedical systems employing inductive links and techniques for employing inductive links for both power and data transfer in a biomedical context.

His research is concerned primarily with biomedical wireless power telemetry systems, but his interests also include inductive link modeling, oscillators, and more general power converter and mixed signal design.

**Virgilio Valente** (S'09–M'11) was born in Milan, Italy, in 1979. He received the B.Sc. degree (Hons.) in electronic engineering from the University of York, York, U.K., in 2004, the M.Sc. degree in biomedical engineering from Aalborg University, Aalborg, Denmark, in 2006, and the Ph.D. degree in electronic and electrical engineering from University College London (UCL), London, U.K., in 2011. From 2011 to 2017, he was a Research Associate with the Analog and Biomedical Electronics Group, UCL, during which, in 2015, he also joined Tetrivis Ltd., U.K., as an IC Design Engineer. In 2017, he was a Visiting Scholar with the Nano Lab, Tufts University, USA. He is currently an Assistant Professor (Research) in bioelectronics with the Department of Microelectronics, Delft University of Technology, The Netherlands.

His research interests focus on the development of analog and mixed-mode CMOS integrated circuits for a range of applications, including BioCMOS, lab-on-CMOS and organ-on-chip platforms, implantable and injectable CMOS biosensors, CMOS-microfluidic devices, and smart wireless telemetry systems.

Dr. Valente is a member of the Biomedical Circuits and Systems Technical Committee of the IEEE Circuits and Systems Society. He was a recipient of the 2017 EPSRC IRC i-sense Mobility Fellowship.

**Andreas Demosthenous** (S'94–M'99–SM'05–F'18) received the B.Eng. degree in electrical and electronic engineering from the University of Leicester, Leicester, U.K., in 1992, the M.Sc. degree in telecommunications technology from Aston University, Birmingham, U.K., in 1994, and the Ph.D. degree in electronic and electrical engineering from University College London (UCL), London, U.K., in 1998. He is currently a Professor with the Department of Electronic and Electrical Engineering, UCL, where he also leads the Analog and Biomedical Electronics Group. He has authored over 300 articles in journals and international conference proceedings, several book chapters, and holds several patents. His research interests include analog and mixed-signal integrated circuits for biomedical, sensor, and signal processing applications. He has made outstanding contributions to improving safety and performance in integrated circuit design for active medical devices, such as spinal cord and brain stimulators.

He is a member of the Technical Programme Committee of several IEEE conferences, including the European Solid-State Circuits Conference and the International Symposium on Circuits and Systems. He is currently the Editor-in-Chief of the IEEE TRANSACTIONS ON CIRCUITS AND SYSTEMS–I, an Associate Editor of the IEEE TRANSACTIONS ON BIOMEDICAL CIRCUITS AND SYSTEMS, and serves on the International Advisory Board of Physiological Measurement.

Dr. Demosthenous is a fellow of the Institution of Engineering and Technology and a Chartered Engineer.